12

Examples

In this chapter we illustrate some of the ideas of radiation transport and hydrodynamics coupled with radiation transport by means of a small selection of examples. As described in the introduction, the challenging applications of the theory are left for the technical literature, and the problems presented here have been chosen for their simplicity or pedagogical value.

12.1 Marshak wave and evaporation fronts

The classic example of nonlinear radiation diffusion is the Marshak wave, first discussed by Marshak (1958). It is a self-similar thermal wave, treated with the thermal diffusion approximation, for a material with a constant specific heat and for which the Rosseland mean opacity varies as a power of the temperature. Hydrodynamic motion is ignored. This assumption is unrealistic, but is made for simplicity. This "thermal wave" is not a wave in the sense we used earlier; it does not come from a hyperbolic system of PDEs, and the dispersion relation does not yield wave speeds ω/k, etc. It is a wave in the sense that there is a characteristic structure, in this case a sharp temperature front, that moves through the material in the course of time, of which the shape remains fairly constant. The propagation law is not distance $\propto$ time, as expected for a hyperbolic system, but distance $\propto$ time$^{1/2}$ instead, owing to its diffusion nature.

A thorough discussion of how the thermal diffusion solution to this problem compares with transport solutions is given in Mihalas and Mihalas (1984), Section 103. Zel'dovich and Raizer (1967) devote Chapter 10 to thermal waves in general, and Section 7 to the Marshak problem. Pomraning gives an analytic solution in a linear case with $\kappa =$ constant and $C_v \propto T^3$ using nonequilibrium diffusion (Eddington approximation) and transport (Pomraning, 1979; Ganapol and Pomraning, 1983). Larsen and Pomraning (1980) use asymptotic analysis to obtain a system one order more accurate than thermal diffusion, using which it can be

explained why the diffusion Marshak front speed is too great. Su and Olson (1996) present accurate solutions to Pomraning's linear problem in the Eddington approximation.

The geometry of the problem is a slab of material located in $z \geq 0$, and it is initially at zero temperature. Starting at time zero, radiation is applied at the $z = 0$ interface that is a blackbody at $T = T_0$, and this remains constant thereafter. This is one of those instances where the somewhat unphysical boundary condition is applied that the total energy density is specified, $E = aT_0^4$ in this case. It would be more sensible to require that the *incoming* radiation be the hemisphere flux σT_0^4, since the flux that comes back out from the problem is less, but that boundary condition makes the problem nonself-similar. We proceed with the simple boundary condition, and after all, the example is intended only to "guide the insight."

We let ρ be the material density and C_v be the specific heat, both constant. The thermal diffusion formula is used, so the flux is

$$F = -\frac{16\sigma T^3}{3\kappa_R \rho}\frac{\partial T}{\partial z}. \tag{12.1}$$

The opacity κ_R is assumed to follow a power law:

$$\kappa_R = \kappa_R(T_0)\left(\frac{T}{T_0}\right)^{-n}. \tag{12.2}$$

The exponent n will be set to either $n = 0$, which describes electron scattering, or to $n = 3$, which is representative of bound–free and free–free absorption. One thing to notice is that it is the opacity for temperatures near T_0 that is being represented in this way, not the opacity of the cold material in the slab at the start. When the formula for the opacity is put into (12.1) it becomes

$$F = -\frac{16\sigma}{3(n+4)T_0^n \kappa_R(T_0)\rho}\frac{\partial T^{n+4}}{\partial z}, \tag{12.3}$$

where the powers of T in the diffusivity have been combined with the T inside the gradient. The diffusion equation for the temperature follows directly from this, and is

$$\frac{\partial T}{\partial t} = \frac{1}{\rho C_v}\frac{\partial}{\partial z}\left(\frac{16\sigma}{3(n+4)T_0^n \kappa_R(T_0)\rho}\frac{\partial T^{n+4}}{\partial z}\right). \tag{12.4}$$

The temperature scaled by T_0 is the self-similar dependent variable for this problem,

$$g \equiv \frac{T}{T_0}, \tag{12.5}$$

and an inspection of the equation suggests that

$$\xi = \frac{K}{\sqrt{t}}\, z \tag{12.6}$$

be the scaled independent variable, with a suitable constant factor K. Collecting the constants in the equation gives this result

$$-\xi \frac{dg}{d\xi} = \frac{d^2 g^{n+4}}{d\xi^2}, \tag{12.7}$$

provided K is defined to be

$$K = \left(\frac{3(n+4)\kappa_R(T_0)\rho^2 C_v}{32\sigma T_0^3} \right)^{1/2}. \tag{12.8}$$

Equation (12.7) is to be solved with the boundary condition that $g = 1$ at $\xi = 0$, and another condition that is consistent with the material ahead of the thermal wave being at zero temperature. It will be seen that the solutions of (12.7) go to exactly zero at a finite value of ξ, which we will call $\xi_{\max}$. There are an infinite number of solutions that go to zero at a particular $\xi_{\max}$, but for all but one of these the flux tends to a nonzero value in the limit $\xi \to \xi_{\max}$. That it should be zero seems obvious physically, but it also follows from (12.7) if we integrate from a value $\xi < \xi_{\max}$ to a value of ξ located in the zero-temperature region ahead of the front. An integration by parts of the left-hand side leads to

$$\xi g + \int_{\xi}^{\infty} g\, d\xi = -\frac{dg^{n+4}}{d\xi}. \tag{12.9}$$

The left-hand side clearly tends to zero as $\xi \to \xi_{\max}$, so the right-hand side, which is proportional to the flux, must tend to zero also. We can determine the behavior of g near the front by approximating the left-hand side of (12.9) with $\xi_{\max} g$, which leads to the form

$$g \sim \left[\frac{(n+3)\xi_{\max}}{n+4} (\xi_{\max} - \xi) \right]^{1/(n+3)}. \tag{12.10}$$

This relation is the actual boundary condition at $\xi = \xi_{\max}$, and used in conjunction with $g = 1$ at $\xi = 0$ it determines a unique solution. The value of $\xi_{\max}$ must be adjusted by trial and error until an integration from $\xi_{\max}$ to 0, started with the correct limiting form at the front, gives $g = 1$ at $\xi = 0$.

The values found for $\xi_{\max}$ are 1.232 for $n = 0$ and 1.121 for $n = 3$. The scaled temperature distributions for these two cases are shown in Figure 12.1. We see that for the higher value of n the temperature profile is closer to a square shape. In fact, the degree of squareness is remarkable. Almost all the material that has

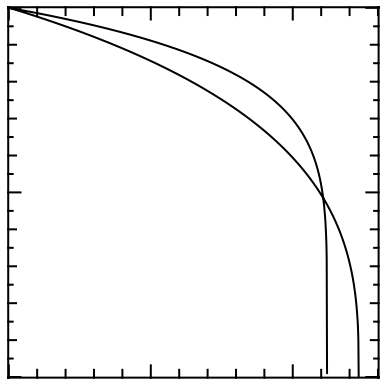

Fig. 12.1 Self-similar temperature distributions for Marshak waves with $\kappa_R \propto T^{-n}$. Abscissa: scaled distance from boundary. Ordinate: scaled temperature g.

been heated by the wave is at a temperature close to T_0, and the drop occurs very abruptly just at the front. This is a consequence of the "bleaching" associated with the wave. The material, very opaque to start with, becomes transparent as it is heated. Not totally so, but sufficiently transparent to allow the flow of radiation to equalize the temperature.

The flux is recovered from the solution by substituting the similarity variables into (12.1). The result is

$$F = -F_1 \frac{dg^{n+4}}{d\xi}, \tag{12.11}$$

where F_1 is the scaling value of the flux,

$$F_1 = \left[\frac{8(n+4)\sigma T_0^4 \rho C_v T_0}{3\kappa_R(T_0)\rho t} \right]^{1/2}. \tag{12.12}$$

The numerical solutions for the flux in units of F_1 for the $n = 0$ and $n = 3$ cases are shown in Figure 12.2. The other scale for flux we think about is $F_0 = cE_0 = 4\sigma T_0^4$, and if the flux is scaled to that we find

$$\frac{F}{cE_0} = -\left[\frac{(n+4)\rho C_v T_0 \lambda_R(T_0)}{6\sigma T_0^4 t} \right]^{1/2} \frac{dg^{n+4}}{d\xi}, \tag{12.13}$$

The ratio $\rho C_v T_0 \lambda_R(T_0)/\sigma T_0^4 t$ that appears here has a physical interpretation: it is the comparison of the heat content of a layer one Rosseland mean free path thick (at T_0) with the energy received from a blackbody at T_0 in the time t. If the

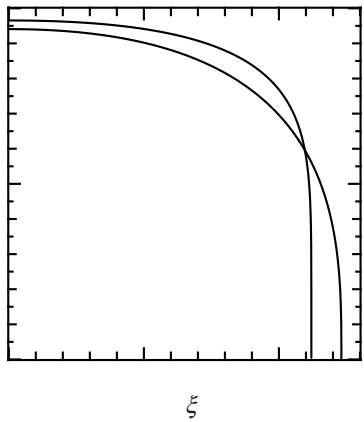

Fig. 12.2 Self-similar flux distributions for Marshak waves with $\kappa_R \propto T^{-n}$. Abscissa: scaled distance from boundary. Ordinate: flux in similarity unit F_1 defined in the text.

ratio is small, enough heat has been absorbed to warm a layer many mean free paths thick. This means that the absorption of heat slows down and the net flux across the $z = 0$ boundary is diminished. If the ratio is large then presumably the front cannot have penetrated even one mean free path. This means that the thermal diffusion approximation is poor. We see that in values of F/cE_0 that are larger than unity. In other words,

$$t > \frac{(n+4)\rho C_v T_0 \lambda_R(T_0)}{6\sigma T_0^4} \tag{12.14}$$

is a condition for this model to be valid. We also see the validity condition by substituting K back into the relation giving the scaling of z:

$$z = \lambda_R(T_0)\left[\frac{32\sigma T_0^4 t}{3(n+4)\rho C_v T_0 \lambda_R(T_0)}\right]^{1/2} \xi. \tag{12.15}$$

Thus the front will have penetrated several mean free paths only if the time obeys the condition (12.14).

Even when the time is late enough to obey condition (12.14) the flux can still violate $F < cE$ because F decreases toward the front much less steeply that $E \propto T^4$ does. The self-similar profile of F/cE is shown in Figure 12.3. This scaling function reaches values of 10–20 before the front is approached even moderately closely. As a result condition (12.14) would have to be obeyed by a large factor, perhaps 100 or more, for $F < cE$ to be satisfied over most of the heated region. Mihalas and Mihalas (1984) illustrate other calculations of the Marshak problem

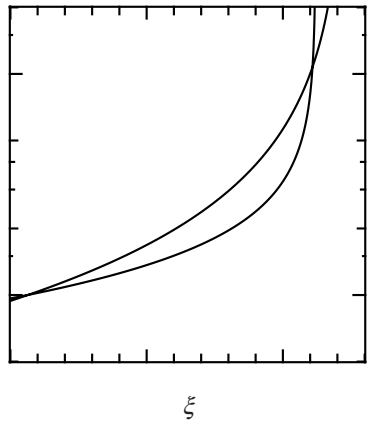

Fig. 12.3 The similarity function giving the profile of F/cE vs scaled distance.

for which the radiation transport approximation has been improved, either by using a flux limiter or by doing accurate angle-dependent transport. These results support the factor 100 suggested here. In particular applications it is possible that the condition is adequately satisfied, but that certainly should be checked before making rough estimates based on Marshak scaling.

The simple Marshak theory presented here is extended in another way by Hammer and Rosen (2003); rather than considering transport and multifrequency modifications to the theory, they present a simple asymptotic method that provides an analytic solution and that can be extended to consider subsonic thermal waves and materials with real physical properties – specific heat and opacity – in place of the power-law relations we have considered.

A problem that is related in some ways to the Marshak problem is evaporation of a cold spherical cloud that is immersed in a hot surrounding medium. This problem was originally treated by Cowie and McKee (1977) and is a central part of the multiphase model of the interstellar medium. A subsequent paper (Mckee and Cowie, 1977) incorporates the cooling effect of (optically thin) radiation. In the Cowie and McKee model the heat flux is caused by thermal conduction, not by radiation diffusion, but the analysis is just the same. The interior of the cloud is treated as cold and dense, and the evaporation front progresses into the cloud so slowly that a reasonable approximation is a steady outflow of the heated material. This flow begins near the front at a negligible speed and accelerates outward and in fact becomes transonic. It reaches quite high velocities far from the cloud. The temperature starts from some low value at the front and also increases outward, but it levels off far from the cloud at the temperature of the surrounding medium. This set of assumptions is not appropriate for all conditions when

a cold cloud is embedded in a hot medium, but it may have some domain of applicability.

The problem is described by the steady-flow equations, in spherical symmetry, for the conservation of mass, momentum, and energy. The thermal conduction enters only in the last equation. If the outflow velocity is u, the density is ρ and the pressure is represented as $p = \rho a^2$, where a is the isothermal sound speed, then taking F_c for the conduction flux, the conservation laws are

$$\rho u r^2 = \frac{\dot{\mathcal{M}}}{4\pi}, \tag{12.16}$$

$$u\frac{du}{dr} + \frac{a^2}{\rho}\frac{d\rho}{dr} + \frac{da^2}{dr} = 0, \tag{12.17}$$

$$\frac{1}{2}u^2 + \frac{5}{2}a^2 + \frac{4\pi r^2 F_c}{\dot{\mathcal{M}}} = 0. \tag{12.18}$$

The conduction flux is obtained using a law like Spitzer's (Spitzer and Härm, 1953), but neglecting the variation of the Coulomb logarithm:

$$F_c = -K_S T^{5/2}\frac{dT}{dr}, \tag{12.19}$$

which we put in terms of the sound speed as

$$F_c = -K_S \mathcal{R}^{-7/2}(a^2)^{5/2}\frac{da^2}{dr}. \tag{12.20}$$

(Here $\mathcal{R}$ is the gas constant divided by the mean atomic weight.) Using this relation we can solve (12.18) for da^2/dr and obtain

$$\frac{da^2}{dr} = \frac{A}{(a^2)^{5/2}r^2}(u^2 + 5a^2), \tag{12.21}$$

where A is the collection of constants

$$A = \frac{\dot{\mathcal{M}}\mathcal{R}^{7/2}}{8\pi K_S}. \tag{12.22}$$

Eliminating ρ from the momentum equation (12.17) using the mass equation (12.16) leads to this form of the acceleration equation, very familiar from stellar wind theory:

$$\frac{1}{2}\left(1 - \frac{a^2}{u^2}\right)\frac{du^2}{dr} - \frac{2a^2}{r} + \frac{da^2}{dr} = 0. \tag{12.23}$$

Our strategy now is the following. What we know is that the velocity and temperature go to negligible values as $r \to R_0$, which is the radius for the cold cloud, and which we assume is given. We also know that the temperature goes to a value

T_∞ as $r \to \infty$, which means that $a \to a_\infty$. We do *not* know the evaporation rate $\dot{\mathcal{M}}$, and that is one major thing we want to find out, which means that A is an eigenvalue for the problem.

The initial attack is to make scale transformations of radius and velocity so that after scaling the sonic point, where $u = a$, is at unit radius, and both u and a are unity there. We forthwith adopt that scaling without changing the labels for the variables. We will put the proper units back in later. The first thing we observe is that since r, u, and a are all one at the sonic point, then if du^2/dr is to be finite there, as it must be if there *is* a transonic flow, then it must be true that

$$\left(\frac{da^2}{dr}\right)_s = 2 \tag{12.24}$$

for the sonic point value. That immediately determines A in the scaled units (but *not* in natural units),

$$A = \frac{1}{3}, \tag{12.25}$$

which means that the energy equation takes this form with no unknown coefficients:

$$\frac{da^2}{dr} = \frac{1}{3(a^2)^{5/2}r^2}(u^2 + 5a^2). \tag{12.26}$$

The rest of the solution method consists of solving (12.23) and (12.26) as a system, beginning with the sonic point conditions and integrating each way in radius. The sonic point is a singular point, of course, and the integration subroutines blow up if the integration is actually begun *at* the sonic point. It is necessary to take a small step away in the direction the integration should go. But what slope should be assumed for u^2? This requires an application of L'Hospital's rule:

$$\left(\frac{du^2}{dr}\right)_s = 2\lim_{r\to 1}\frac{2a^2/r - da^2/dr}{1 - a^2/u^2} = 2\frac{d(2a^2/r - da^2/dr)/dr}{d(1 - a^2/u^2)/dr}. \tag{12.27}$$

The derivatives are carried out using (12.26) to obtain the second derivative of a^2 and leaving the first derivative of u^2 as an unknown. What is found is

$$(u^2)' = 2\frac{38/3 - (u^2)'/3}{(u^2)' - 2}, \tag{12.28}$$

a quadratic equation that has the roots

$$(u^2)' = \frac{2}{3}(1 + \sqrt{58}), \qquad \frac{2}{3}(1 - \sqrt{58}), \tag{12.29}$$

from which we have to select the positive root for an accelerated flow.

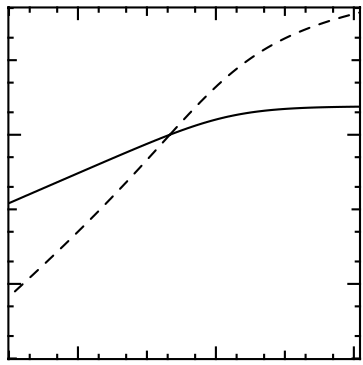

Fig. 12.4 Scaled temperature (solid curve) and velocity (dashed curve) vs radius for transonic evaporation.

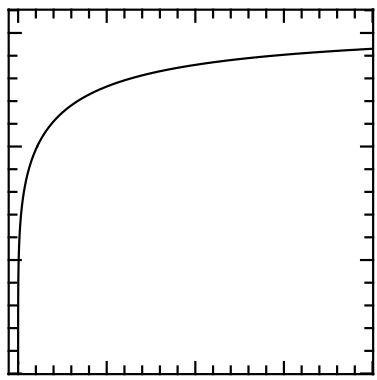

Fig. 12.5 Scaled temperature near the sonic point for transonic evaporation.

Now we simply do the numerical integrations and tabulate u^2 and a^2 as functions of radius. We find that u^2 and a^2 vanish at $r = 0.823$ in sonic radius units, which means that the true location of the sonic point is

$$\frac{r_s}{R_0} = \frac{1}{0.823} = 1.215. \tag{12.30}$$

The distributions of velocity and temperature are shown in Figures 12.4 and 12.5.

The squared sound speed has the asymptotic value at large r of 2.380, which means that the sonic point temperature is

$$T_s = 0.420 T_\infty. \tag{12.31}$$

Restoring A to its natural units gives

$$A = \frac{1}{3} a_s^5 r_s, \tag{12.32}$$

which means that the evaporation rate is

$$\begin{aligned} \dot{\mathcal{M}} &= \frac{8\pi K_S}{\mathcal{R}^{7/2}} A = \frac{8\pi (a_s/a_\infty)^5 (r_s/R_0) R_0 K(T_\infty)}{3\mathcal{R}} \\ &= 0.0927 \frac{4\pi R_0 K(T_\infty)}{\mathcal{R}}. \end{aligned} \tag{12.33}$$

Just for fun, we put in the radius of the sun and a rough estimate, 1.5×10^6 K, for the coronal temperature, and derive an evaporation rate of $2.9 \times 10^{-14}\, \mathcal{M}_\odot\, \mathrm{y}^{-1}$, which is in the right ballpark compared with the sun's mass-loss rate!

We also find that in the subsonic part of the flow, where $u \ll a$, the pressure tends to a constant value. This pressure is the reaction to the outflowing material, i.e., it is due to the "rocket effect". This pressure turns out to be

$$p_{\mathrm{sub}} = 1.0085 \frac{\dot{\mathcal{M}} (\mathcal{R} T_\infty)^{1/2}}{4\pi R_0^2} = 0.0935 \frac{K(T_\infty) T_\infty^{1/2}}{R_0 \mathcal{R}^{1/2}}. \tag{12.34}$$

This has the order of magnitude of the conduction flux for temperature T_∞, if the temperature gradient is T_∞ / R_0, divided by the sound speed at T_∞. For the solar example the pressure turns out to be 4×10^{-4} dyne cm^{-2} corresponding to a particle density of 2×10^6 cm^{-3}, which is on the low side for the base of the corona, but perhaps not too bad for coronal holes. The flow speed continues to rise at large r as expected from Bernoulli's law, since in isothermal conditions the work function is the Helmholtz free energy, which goes logarithmically to $-\infty$ as $\rho \to 0$. At $r = 100 R_0$ the velocity is around $6 a_s$, which for the corona example is 820 km s^{-1}. This is large, but not by more than a factor 2.

The fact that these estimates for the mass loss from the corona are not completely outrageous, even though gravity has been neglected in this model, demonstrates that thermal conduction is a major ingredient in the solar wind, although only one part of the total picture. The conduction-dominated model of the solar wind is the one of Chamberlain (1960, 1961), although transonic solutions were considered later by Noble and Scarf (1962). These models stand in contrast to Parker's original wind model, for which conduction is ignored (Parker, 1960). A good review of the subject is found in Brandt (1970).

12.2 Ionization fronts

A structure that occurs in stars and nebulae that is like a shock wave in several respects, but also has characteristics in common with the Marshak wave, is the ionization front. (See Kahn (1954), Axford (1961), and Mihalas and Mihalas (1984).) We are considering radiation hydrodynamic behavior of a system made up of the typical cosmic mixture, which is mostly hydrogen. We suppose that there is a quite sizable radiative flux, $\mathbf{F}$, flowing through the system. The facts that: (1) hydrogen usually ionizes around $T = 10^4$ K in LTE; (2) the hydrogen opacity is sharply increasing with T when hydrogen is neutral, but decreases with T when hydrogen is ionized; and (3) thermal relaxation causes the radiation flux to tend to a spatially constant value combine to create a spatial profile of the temperature that has a sharp step around 10^4 K. This is a consequence of the diffusion formula, according to which $\nabla T \propto \kappa_R(T)\rho F/T^3$, but is observed even when the diffusion approximation is not applicable. The temperature has a sharp step even when the flux is not actually constant, provided F varies between two fixed positive limits. Not infrequently the region on one side that is mostly neutral will relax to one constant value of the flux while the mostly ionized region on the other side will have relaxed to a different value. The two values of F remain different since the high opacity and high specific heat (due to ionization) of the $T \approx 10^4$ K material makes this an insulating barrier.

The concept of an "ionization front" emerges if we imagine that the opacity in a certain temperature range, say 7000–15 000 K, is some enormous value, and otherwise is what it is supposed to be. This idealization makes the temperature jump discontinuously from 7000 K to 15 000 K across some surface in space, the ionization front. In reality the opacity is large but not infinite in this range, and the thickness of the front is not zero, but something that depends on the magnitude of $\kappa_R(T)\rho F/T^4$. The idealization may be useful in cases for which the true thickness is quite small compared with other length scales.

This discussion has been based on the assumption of LTE, and in particular on the validity of the Saha equation which determines the degree of ionization in terms of the temperature. This is the appropriate regime for stars, but not for nebulae. Out of LTE we have to regard the ionization fraction of hydrogen, x, as an additional degree of freedom that is determined by the equation for ionization kinetics. In this case, too, it may happen that the scale length for x to jump from a value $\ll 1$ to nearly 1 may be short compared with other length scales. We can use the ionization front picture here as well, but for this case the "neutral" and "ionized" states are not strictly tied to particular values of the temperature, although the values 7000 K and 15 000 K are reasonable.

In neither the LTE nor the non-LTE case is the ionization transition actually a phase transition in the thermodynamic sense. In the latter picture the two phases

can coexist only on a certain curve in (p, T) space, whereas the neutral and ionized species are present to a greater or lesser degree at all p and T. But in a broad-brush way, when we ignore the small neutral fraction in a mostly ionized plasma or the small ionized fraction in a mostly neutral gas, there is some similarity, and the quantity analogous to the latent heat is the ionization potential of hydrogen expressed per unit mass of material. This has the large value $1.302 \times 10^{13}\,\mathrm{erg\,g^{-1}}$ for the cosmic mixture with a hydrogen mass fraction $X = 0.7$. This is equivalent to the specific kinetic energy for a flow velocity of $51\,\mathrm{km\,s^{-1}}$. For flows with $u \ll 50\,\mathrm{km\,s^{-1}}$ the ionization energy and the radiative flux are the largest terms in the energy budget.

We continue the discussion of ionization fronts by considering the jump conditions that express the conservation laws for mass, momentum, and energy when there is a locally-steady flow through the front. What "locally-steady" means is that changes are small in the time required for a parcel of mass to pass through the front. We assign specific temperatures to the neutral (#1) side and the ionized (#2) side of the front, 7000 K and 15 000 K, respectively, so the isothermal sound speeds are $a_1 \approx 7\,\mathrm{km\,s^{-1}}$ and $a_2 \approx 13\,\mathrm{km\,s^{-1}}$. The ideal gas law for a $\gamma = 5/3$ gas is assumed, except that the ionized gas has an internal energy that is larger than that of the neutral gas by an increment I_H, the ionization energy per unit mass $\approx 1.302 \times 10^{13}\,\mathrm{erg\,g^{-1}}$. The jump conditions are then

$$\rho_1 v_1 = \rho_2 v_2 = C_1, \tag{12.35}$$

$$p_1 + \rho_1 v_1^2 = p_2 + \rho_2 v_2^2, \tag{12.36}$$

$$\left(\frac{5}{2}\frac{p_2}{\rho_2} + I_H + \frac{1}{2}v_2^2\right) - \left(\frac{5}{2}\frac{p_1}{\rho_1} + \frac{1}{2}v_1^2\right) = \frac{\Delta F}{C_1}. \tag{12.37}$$

Our discussion of the magnitude of I_H suggests that for relatively low-velocity flows the kinetic energy and enthalpy terms may be neglected in the energy jump condition, which then becomes a relation that fixes the mass flux through the front in terms of the jump in the radiative flux.

The possible solutions of the mass and momentum jump conditions are represented as the relations between the compression ratio, $\eta \equiv \rho_2/\rho_1 = v_1/v_2$, and the (isothermal) Mach numbers on the neutral side $M_1 \equiv v_1/a_1$ and the ionized side $M_2 \equiv v_2/a_2$,

$$M_1^2 = \frac{\eta(\eta(a_2/a_1)^2 - 1)}{\eta - 1}, \tag{12.38}$$

$$M_2^2 = \frac{\eta - (a_1/a_2)^2}{\eta(\eta - 1)}. \tag{12.39}$$

These relations are shown in Figure 12.6.

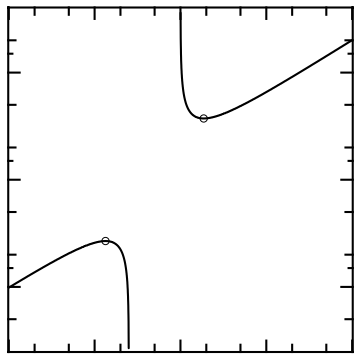

Fig. 12.6 Relation between neutral Mach number v_1/a_1 (ordinate) and compression $\eta = \rho_2/\rho_1$ (abscissa) for ionization fronts with $a_2/a_1 = 13/7 = 1.87$. The labels "R" and "D" distinguish the two branches, and each branch has a "weak" and a "strong" side, as shown. Circles mark the apex of each branch, where $M_2 = 1$.

The relation in Figure 12.6 indicates how ionization fronts are classified into four types. The upper branch corresponds to those fronts that are supersonic on the neutral side and the lower branch consists of the fronts that are subsonic on the neutral side. The "weak" fronts consist of those for which the compression is closer to unity – and the "strong" ones for which the compression is further from unity – at a given neutral Mach number. The weak fronts have the same character, supersonic or subsonic, on both sides, while for the strong fronts the supersonic/subsonic character is reversed for the two sides.

If a value for the flux jump ΔF is specified, and if ρ_1 is given, then there is an implied value of C_1 and therefore of v_1. We speak of *R-type conditions* when the implied v_1 falls in the range of R-type fronts, of *D-type conditions* when the implied v_1 falls in the range of D-type fronts, and of *M-type conditions* when the implied velocity falls in the gap between the two branches. This gap is the Mach number range 0.29–3.42 for $a_2/a_1 = 1.87$. M-type conditions cannot simply produce an ionization front with a suitable speed, but something else must happen. This is generally the creation of a shock that alters the conditions on the neutral side so that D-type or R-type conditions are met. If the shock is as weak as possible, so the D-type or R-type conditions are *barely* met, then these will be D-critical or R-critical, i.e., at one of the apex points where the ionized Mach number is unity.

There is a close parallel between ionization fronts and combustion fronts. The latter occur when the material contains chemically reacting species, and when the constituents are mostly unreacted on one side of the front while the reaction is

nearly complete on the other side. If label 1 is associated with unreacted material and label 2 is associated with reacted material, then the jump conditions are the same as equations (12.35)–(12.37), except that the combination $\Delta F/C_1 - I_H$ is replaced by the heat of reaction ΔH. The solutions are qualitatively like those for the ionization front: there are supersonic combustion fronts, which are called *detonations*, and subsonic combustion fronts, which are called *deflagrations*, and each type can be weak or strong, based on the Mach number on the burnt side. Combustion processes that include a critical front, for which the flow speed is just sonic on the burnt side, are called Chapman–Jouget processes.

Because the radiation field is (presumably) negligible for combustion fronts, the second law of thermodynamics and chemical kinetics considerations lead to constraints on combustion fronts that do not apply to ionization fronts. These include the following: the flow must be in the #1–#2 direction, so the reaction goes in the exothermic direction when mass passes through the front; strong deflagrations (D-fronts) and weak detonations (R-fronts) are impossible. A weak detonation case always leads to a precompressing shock and a critical detonation. This is the Jouget hypothesis, and it makes the properties of the Chapman–Jouget detonation of prime importance in modeling explosives. This question is addressed in Landau and Lifshitz (1959), Sections 121–122, and also Zel'dovich and Raizer (1967). It is also treated from a slightly different viewpoint in Courant and Friedrichs (1948). The essential difference between ionization fronts and combustion fronts is that the latter are everywhere in thermal equilibrium, while ionization fronts are modified by the nonequilibrium radiation flux.

In order to understand better how an ionization front affects the surrounding flow, we can count the number of C_+ or C_- characteristics that can reach a point on the neutral side and on the ionized side of the front. We recall that for a shock wave, two characteristics reach the preshock side of the shock front, and just one reaches the shock from the postshock side. A C_0 characteristic also supplies the preshock entropy. There are five mechanical variables needed to describe the state of the fluid on each side of the shock and the shock's motion; these are u_1, ρ_1, u_2, ρ_2, and u_S. The data provided by the three acoustic characteristics, plus the two mechanical jump conditions, just determine these five variables. The two additional thermodynamic variables, the pre- and post-shock entropies, match the data from the C_0 characteristic and the energy jump condition. So shocks are fully determined. In particular, the details of the internal structure of the shock cannot influence the surrounding flow.

The count of just the mechanical (C_+ and C_-) characteristics reaching each side of an ionization front is given in Table 12.1, where we distinguish an advancing front, for which the flow is from the neutral side to the ionized side, from a receding front. We have the same five mechanical variables, and we have two

Table 12.1. *Count of characteristics at ionization fronts*

type		advancing	receding
R	weak	2 neutral, 0 ionized	0 neutral, 2 ionized
	strong	2 neutral, 1 ionized	0 neutral, 1 ionized
D	weak	1 neutral, 1 ionized	1 neutral, 1 ionized
	strong	1 neutral, 0 ionized	1 neutral, 2 ionized

mechanical jump conditions; the energy jump condition gives an additional constraint if the value of ΔF is imposed. This means that if there are two C_+ and C_- characteristics the flow including the ionization front with a specified ΔF is just determined; if there are less than two characteristics it is underdetermined, and if there are more than two it is overdetermined. What we see from an examination of Table 12.1 is that the weak fronts of either type, whether advancing or receding, are just determined. The advancing strong R and receding strong D fronts are overdetermined, and such flows may resolve into critical fronts followed by a rarefaction (advancing strong R) or preceded by a shock (receding strong D). The underdetermined cases, advancing strong D and receding strong R, may be truly dependent for their behavior on the details of the internal structure of the front. The advancing weak-R and both advancing and receding weak-D type ionization fronts are the ones often encountered in simulations of H II regions and stellar atmospheres, respectively.

12.3 Comptonization

In this section we consider those corrections to the statements made earlier that the frequency change in Compton (or Thomson) scattering is negligible, and that such scattering has no effect on the energy exchange between radiation and matter. These may be fair approximations, but they cannot be true in general. If this were so, we could put 10^{12} photons sampled from a blackbody distribution at 10^5 K in a 1 cm^3 box together with 10^{12} electrons with a kinetic temperature of 10^4 K and they would remain at their respective temperatures forever. We do not think this happens with billiard balls, why should it happen with electrons and photons? The collisions between billiard balls, when the balls bounce off each other at some angle of scattering, result in the exchange of energy and momentum between the colliders, just in order to satisfy the conservation laws. This is all it takes to result in equilibration of the two species.

It is just so with scattering of photons by electrons. We will look more closely at the relations for scattering of an arbitrary intensity field by a thermal-equilibrium

electron gas. We will introduce a new function $R(\nu, \nu')$, the redistribution function for Compton scattering. Actually, we saw such a function in the discussion of partial redistribution in line scattering, and many of the properties of R are similar for the two kinds of scattering. The definition of R is this: a radiation field of low intensity (which means: ignore stimulated emission) that has an angle-averaged intensity $J_{\nu'}$, and therefore for which the energy density in the bandwidth $d\nu'$ is $4\pi J_{\nu'} d\nu'/c$, produces an emissivity due to this band in a band $d\nu$ at a distinct frequency ν equal to

$$N_e \sigma_T R(\nu, \nu') J_{\nu'} d\nu d\nu'. \tag{12.40}$$

The choice of σ_T here as the scaling cross section is just a convenience. The frequency dependence of the cross section is contained in R. The definition of R involves the *energy* of the source photons and the *energy* of the emitted photons rather than the photon numbers. Therefore R is related to the differential cross section with respect to final photon frequency as follows:

$$\sigma_T R(\nu, \nu') = \frac{\nu}{\nu'} \frac{d\sigma(\nu', \nu)}{d\nu}. \tag{12.41}$$

Notice that in $R(\nu, \nu')$ the first argument is the frequency of the photon after scattering, and the second argument is the frequency before scattering.

Recall the definition of the modal photon density n_ν: $n_\nu = (2h\nu^3/c^2)^{-1} J_\nu$, for the mean number per mode after integrating over solid angle. The equation for the rate of change of the modal density due just to scattering, when account is taken of the in-scatterings as well as the out-scatterings and the stimulated scattering factors are now included as in the discussion in Section 8.3, is this (cf. Section 4.2, (4.24)):

$$\frac{1}{N_e \sigma_T c} \frac{\partial n_\nu}{\partial t} = \frac{c^2}{2h\nu^3} \int_0^\infty d\nu' \Bigg[- R(\nu', \nu) \frac{\nu}{\nu'} J_\nu \left(1 + \frac{c^2 J_{\nu'}}{2h\nu'^3}\right) + R(\nu, \nu') J_{\nu'} \left(1 + \frac{c^2 J_\nu}{2h\nu^3}\right) \Bigg]. \tag{12.42}$$

Before proceeding we have to consider what kind of symmetry is possessed by the function R. Earlier it was stated that R is symmetric under exchange of ν and ν'. We will see that this is *almost* true, by the following argument. Consider a thought experiment in which some radiation is introduced into a sealed box, with perfectly reflecting walls, containing thermal electrons at a temperature T, and the radiation is allowed to come to equilibrium with them; however, no sources or sinks of radiation exist within the box – the same billiard-ball picture mentioned above. When the radiation is at equilibrium, it must be described by a Bose–Einstein distribution at the temperature T of the scatterers, with a fugacity z

that depends on the fixed number of photons in the box:

$$J_\nu = \frac{2h\nu^3/c^2}{z\exp(h\nu/kT) - 1}. \tag{12.43}$$

For this value of the intensity, the stimulation factor $1 + n$ becomes $z/[z - \exp(-h\nu/kT)]$. Therefore, if the intensity has the form given by (12.43), the photon gains and losses must exactly balance. The equation that results is

$$\begin{aligned}\int d\nu' R(\nu, \nu') &\frac{\nu'^3}{[z\exp(h\nu'/kT) - 1][z - \exp(-h\nu/kT)]} \\ &= \int d\nu' R(\nu', \nu)\frac{\nu^4}{\nu'}\frac{1}{[z\exp(h\nu/kT) - 1][z - \exp(-h\nu'/kT)]}.\end{aligned} \tag{12.44}$$

A rearrangement yields

$$\begin{aligned}\int d\nu' &\left[R(\nu, \nu') - \left(\frac{\nu}{\nu'}\right)^4 \exp\left(\frac{h(\nu' - \nu)}{kT}\right) R(\nu', \nu)\right] \\ &\times \frac{\nu'^3}{[z\exp(h\nu'/kT) - 1][z - \exp(-h\nu/kT)]} = 0,\end{aligned} \tag{12.45}$$

which must be true for all z. Therefore the redistribution function has to have this symmetry:

$$R(\nu, \nu') = \left(\frac{\nu}{\nu'}\right)^4 \exp\left[\frac{h(\nu' - \nu)}{kT}\right] R(\nu', \nu). \tag{12.46}$$

In other words, R is symmetric apart from a small bias that is related to the difference between the two frequencies. At high temperature the redistribution favors upshifting the photon frequencies because of the ν^4 factors, but if the temperature is low in comparison with $h\nu/k$ then downshifting is favored. In essence, there will be a small bias tending to bring the photons toward the middle of the Planck distribution at $h\nu = 4kT$.

Now we can put the two R functions in (12.42) in terms of a single one and express the result in terms of modal densities in this form

$$\begin{aligned}\frac{1}{N_e\sigma_T c}\frac{\partial n_\nu}{\partial t} = &\int_0^\infty d\nu' \frac{\nu}{\nu'} R(\nu', \nu) \\ &\times \left\{-n_\nu(1 + n_{\nu'}) + \exp\left[\frac{h(\nu' - \nu)}{kT}\right] n_{\nu'}(1 + n_\nu)\right\}.\end{aligned} \tag{12.47}$$

From our earlier discussion we expect $R(\nu', \nu)$ to be sharply peaked around $\nu' = \nu$, and therefore provided that the radiation field varies smoothly with ν it should be possible to introduce a Taylor series in $\nu' - \nu$ for the function in braces, do the integrals over ν', which will be moments of $(\nu/\nu')R(\nu, \nu')$, and thus express

the right-hand side of (12.47) in terms of the radiation field and its derivatives. This is the Fokker–Planck method. It may be compared with Harrington's method for PRD, described in Section 9.2.1. When carried to the second order in $\nu' - \nu$ the equation that results is the Kompaneets equation (Kompaneets, 1957). The following discussion most nearly follows Pomraning (1973), with parts adapted from Rybicki and Lightman (1979).

We let $F(\nu, \nu')$ be the function in braces in (12.47),

$$F(\nu, \nu') = -n_\nu(1 + n_{\nu'}) + \exp\left[\frac{h(\nu' - \nu)}{kT}\right] n_{\nu'}(1 + n_\nu). \tag{12.48}$$

We form the Taylor expansion of F in the variable ν' around the point ν,

$$F(\nu, \nu') = F_{\nu'}(\nu, \nu)(\nu' - \nu) + \frac{1}{2}F_{\nu'\nu'}(\nu, \nu)(\nu' - \nu)^2 + \cdots, \tag{12.49}$$

where the constant term is seen to vanish. After doing the integrations we find

$$\frac{1}{N_e \sigma_T c}\frac{\partial n_\nu}{\partial t} = A(\nu)F_{\nu'}(\nu, \nu) + \frac{1}{2}B(\nu)F_{\nu'\nu'}(\nu, \nu) + \cdots, \tag{12.50}$$

where the derivatives are

$$F_{\nu'}(\nu, \nu) = \frac{\partial n_\nu}{\partial \nu} + \frac{h}{kT}n_\nu(1 + n_\nu), \tag{12.51}$$

$$F_{\nu'\nu'}(\nu, \nu) = \frac{\partial^2 n_\nu}{\partial \nu^2} + \frac{2h}{kT}(1 + n_\nu)\frac{\partial n_\nu}{\partial \nu} + \left(\frac{h}{kT}\right)^2 n_\nu(1 + n_\nu). \tag{12.52}$$

The quantities $A(\nu)$ and $B(\nu)$ are the moments of the differential cross section,

$$A(\nu) = \frac{1}{\sigma_T}\int_0^\infty d\nu'\,(\nu' - \nu)\frac{d\sigma(\nu, \nu')}{d\nu'}, \tag{12.53}$$

$$B(\nu) = \frac{1}{\sigma_T}\int_0^\infty d\nu'\,(\nu' - \nu)^2\frac{d\sigma(\nu, \nu')}{d\nu'}. \tag{12.54}$$

The exact, relativistic differential cross section is rather ugly. It begins with the Klein–Nishina differential cross section versus initial photon frequency and scattering angle, which apply in the rest frame of the initial electron, which then must be averaged over the relativistic Maxwellian distribution. In order to obtain the differential cross section for specific initial and final frequencies as a function of scattering angle, all measured in the fixed frame, the Doppler shift and aberration constraints for initial and final photons must be applied, and the electron-frame photon coordinates may be integrated out. This becomes a nine-dimensional integral, although it includes seven delta functions. The final two integrations are over an azimuthal angle for the electron velocity, which is easy, and the speed distribution, which can only be done numerically. Efficient routines for doing this

calculation have been developed by Kershaw, Prasad, and Beason (1986). Power-series expansions in the two small quantities $h\nu/mc^2$ and kT/mc^2 have been developed for the differential cross section from which it has been shown that to first order in the two small parameters the moments are given by

$$A(\nu) = \frac{kT}{mc^2}\left(4 - \frac{h\nu}{kT}\right)\nu \tag{12.55}$$

and

$$B(\nu) = \frac{2kT}{mc^2}\nu^2. \tag{12.56}$$

These expressions could be improved using the results for the relativistic regime obtained by Cooper (1971).

The value for B, the mean square frequency shift, is not hard to derive from the nonrelativistic Doppler effect formula without worrying about the Klein–Nishina corrections. As it happens, A can then be calculated from it using the requirement of thermodynamic consistency. When these values for A and B are used with the derivatives from (12.51) and (12.53) in the Fokker–Planck equation (12.50) it becomes

$$\frac{1}{N_e\sigma_T c}\frac{\partial n_\nu}{\partial t} = \frac{kT}{mc^2}\left\{\nu^2\frac{\partial^2 n_\nu}{\partial \nu^2} + \left[4 + \frac{h\nu}{kT}(2n_\nu + 1)\right]\nu\frac{\partial n_\nu}{\partial \nu} + \frac{4h\nu}{kT}n_\nu(n_\nu + 1)\right\}, \tag{12.57}$$

which can be rearranged into the standard Kompaneets form (Kompaneets, 1957)

$$\frac{1}{N_e\sigma_T c}\frac{\partial n_x}{\partial t} = \frac{kT}{mc^2}\frac{1}{x^2}\frac{\partial}{\partial x}\left\{x^4\left[\frac{\partial n_x}{\partial x} + n_x(n_x + 1)\right]\right\} \tag{12.58}$$

in which the frequency variable has been scaled by the temperature,

$$x = \frac{h\nu}{kT}. \tag{12.59}$$

Kompaneets' equation has the expected desirable properties: it is written to precisely conserve photons, since the integral $\int n_x x^2\,dx$ is the photon number density. It must be remembered that this equation is only for the local scattering term; it must be supplemented by the transport term, the $\mathbf{n}\cdot\nabla$ part, in the complete transport equation. Besides conserving photons the Kompaneets equation will give back an exact Bose–Einstein distribution in equilibrium. In that case the frequency-flux vanishes because the equation

$$\frac{\partial n_x}{\partial x} + n_x(n_x + 1) = 0 \tag{12.60}$$

is obeyed exactly by functions

$$n_x = \frac{1}{z\exp(x) - 1}, \tag{12.61}$$

i.e., any Bose–Einstein distribution with the local electron temperature.

If we multiply the Kompaneets equation by x^3 and integrate we get an equation that describes how the mean frequency of the photons evolves with time. It is

$$\frac{d\langle x\rangle}{dt} = N_e\sigma_T c\frac{kT}{mc^2}\left(4\langle x\rangle - \langle x^2\rangle\right). \tag{12.62}$$

So a distribution concentrated initially at low frequency will be boosted exponentially with time according to

$$\langle x\rangle \propto e^y, \tag{12.63}$$

where the parameter y is

$$y = \frac{4N_e\sigma_T ctkT}{mc^2} = \frac{4kTN}{mc^2}, \tag{12.64}$$

where N is the mean number of scatterings that have occurred.

An illustration of the use of the Kompaneets equation is to find the spectral distribution of the photons that begin with a certain frequency in an infinite volume of electrons at a fixed temperature T after a large number N of scatterings. This is also a chance to illustrate some ideas about probability distributions of the number of scatterings and generating functions.

The modal photon density will obey (12.58). The left-hand side is the change of n_x in the mean time between scatterings, so we can regard the right-hand side as the change in n_x per scattering. We write the right-hand side as

$$-n_x + (n_x + K[n_x]), \tag{12.65}$$

where the first term represents the disappearance of the radiation as it was before the event, and the second term is the reappearance of radiation as modified by the Compton scattering process. That is, the first term is the rate of absorption and the second is the rate of reemission. The operator K is the Kompaneets operator, and we will drop the stimulated term, thus making it a linear operator,

$$K[n] \equiv \frac{kT}{mc^2}\frac{1}{x^2}\frac{\partial}{\partial x}\left[x^4\left(\frac{\partial n}{\partial x} + n\right)\right]. \tag{12.66}$$

Now, let us keep track of the photons according to how many times they have scattered. Let $n_0(x,t)$ be what remains of the initial distribution of photons that have survived unscattered until time t. Let $n_1(x,t)$ be those photons that have had one and only one scattering up to time t, and so on. We can write evolution

equations for the groups of photons that look like this:

$$\frac{1}{N_e\sigma_T c}\frac{\partial n_0}{\partial t} = -n_0, \tag{12.67}$$

$$\frac{1}{N_e\sigma_T c}\frac{\partial n_r}{\partial t} = -n_r + n_{r-1} + K[n_{r-1}] \qquad \text{for } r \geq 1. \tag{12.68}$$

The photons in group 0 can only be destroyed, but the photons in groups $1, 2, \ldots$ can be destroyed or created by the action of scattering on the photons in group $r-1$. Now the spectral distribution of photons is determined by how many times they have scattered, but does not change after the last scattering that qualifies them to join that group. Thus the modal density function for photons that have scattered a definite number of times can be expressed as the product of one factor that depends on time and varies as the population of this group grows and decays, and a second factor that depends on frequency, and is the spectrum for all the photons in that group:

$$n_r(x,t) = a_r(t)u_r(x). \tag{12.69}$$

We have noted that the scattering operation does not change the total number of photons, only their frequency distribution, so every function $u_r(x)$ is normalized the same as the initial distribution,

$$\int_0^\infty x^2\,dx\,u_r(x) = \int_0^\infty x^2\,dx\,u_0(x). \tag{12.70}$$

Multiplying (12.68) by x^2 and integrating over x leads to this set of equations for the populations of the groups:

$$\frac{1}{N_e\sigma_T c}\frac{da_0}{dt} = -a_0, \tag{12.71}$$

$$\frac{1}{N_e\sigma_T c}\frac{da_r}{dt} = -a_r + a_{r-1}. \tag{12.72}$$

The K term goes away in the integration since it conserves photons. This set of differential equations is easily solved by recursion, and we find

$$a_r(t) = \exp(-N_e\sigma_T ct)\frac{(N_e\sigma_T ct)^r}{r!}, \tag{12.73}$$

so that at any time t the relative numbers of photons with different numbers of scatterings follow Poisson statistics. The mean number of scatterings in time t is just $N_e\sigma_T ct$.

We are really more interested in the spectral distribution, so we integrate over time in (12.68). We verify that the integral of every $a_r(t)$ is the same as the mean

time between scatterings, $1/N_e\sigma_T c$. The integral of the equation for $r = 0$ vanishes identically, and the other equations give

$$u_r = u_{r-1} + K[u_{r-1}]. \tag{12.74}$$

We want to know about large numbers of scatterings, so this equation would be painful to use for one r after another directly. This is where the generating function concept comes in. We define the generating function, or ϖ transform if you prefer, by

$$\tilde{u} = \sum_{r=0}^{\infty} \varpi^r u_r. \tag{12.75}$$

This would be the spectral distribution of all the photons together if the scattering albedo were ϖ instead of unity. But we do not have to think of ϖ as a real albedo, but can instead handle it as a free parameter. When the typical number of scatterings is so large that we can treat r like a continuous variable, this sum can be approximated by an integral, which is then the Laplace transform of u with respect to r, and the transform variable p is $-\log\varpi$:

$$\tilde{u} = \sum_{r=0}^{\infty} \varpi^r u_r \approx \mathcal{L}_{-\log\varpi}[u]. \tag{12.76}$$

When it is desired to invert the transform to obtain u_r from $\tilde{u}$ this relation can be used:

$$u_r = \frac{1}{2\pi i} \oint \frac{\tilde{u}\, d\varpi}{\varpi^{r+1}}. \tag{12.77}$$

(This is the Cauchy integral formula for the rth derivative of $\tilde{u}$, at $\varpi = 0$, divided by $r!$.) The contour should enclose the origin and not enclose singularities of $\tilde{u}$, such as the point $\varpi = 1$.

Applying the sum operation indicated in (12.75) to (12.74) and noting that the $r = 0$ term is missing leads to

$$\tilde{u} - u_0 = \varpi(\tilde{u} + K[\tilde{u}]). \tag{12.78}$$

We do a little rearrangement of this equation and it takes this form,

$$\tilde{u} = \frac{u_0}{1-\varpi} + \frac{\varpi}{1-\varpi} K[\tilde{u}], \tag{12.79}$$

so the generating function satisfies an inhomogeneous equation with the Kompaneets operator, and the initial distribution is the source.

Working out the derivatives puts the equation in this form:

$$x^2\frac{d^2\tilde{u}}{dx^2} + x(x+4)\frac{d\tilde{u}}{dx} + \left[4x - \frac{mc^2(1-\varpi)}{kT\varpi}\right]\tilde{u} = -\frac{mc^2}{kT}\frac{u_0}{\varpi}. \quad (12.80)$$

With one or two transformations this equation becomes a confluent hypergeometric equation, and we will just quote the answer for the response in the case that the initial distribution is a delta function at $x = x_0$:

$$\tilde{u} = \frac{\Gamma(s)x_0^{s+2}x^s e^{-x}}{\varpi\Gamma(2s+4)}M(s, 2s+4, x_<)U(s, 2s+4, x_>), \quad (12.81)$$

where $x_< = \min(x, x_0)$ and $x_> = \max(x, x_0)$, M and U are the regular and irregular confluent hypergeometric functions, and s, the root of the indicial equation, is

$$s = -\frac{3}{2} + \sqrt{\frac{9}{4} + \frac{mc^2(1-\varpi)}{kT\varpi}}. \quad (12.82)$$

The value of s depends on the Compton y parameter defined in (12.64) in terms of the number of scatterings N. Here we associate N with $\varpi/(1-\varpi)$, so s is related to y by

$$s = -\frac{3}{2} + \sqrt{\frac{9}{4} + \frac{4}{y}}. \quad (12.83)$$

When y is very small, as when the number of scatterings is small, then s is large, and in that case $\tilde{u}$ is very sharply peaked at $x = x_0$. When the y parameter is moderate, then s is moderate also, and an interesting result in that case is if we consider $h\nu_0 \ll kT$. This is the inverse Compton scattering case, because instead of hot photons being degraded by scattering on cold electrons, here cold photons are boosted by scattering on hot electrons. The limiting forms for the M and U functions produce the result that $\tilde{u} \propto x_0^{s+2}x^{-s-3}$ when $x > x_0$. So we get a declining power-law distribution for the scattered spectrum that is flatter and flatter as y becomes larger and s becomes smaller. When $y \gg 1$ then s is small, and the M and U functions tend to unity. What happens in that case is that, whatever the original distribution was, those photons are distributed over a Wien distribution $u \propto e^{-x}$ in the final spectrum. The progression of the spectra of $\tilde{u}$ with y is illustrated in Figure 12.7.

The evolution of $\tilde{u}$ with y is suggestive of how the inverse Compton spectrum changes with time or the number of scatterings, but for a complete picture the inverse ϖ-transform has to be taken. Figure 12.8 shows the time-dependent spectrum for this same case, obtained from a numerical integration of the Kompaneets equation. The suggestion of a power-law spectral distribution in the range

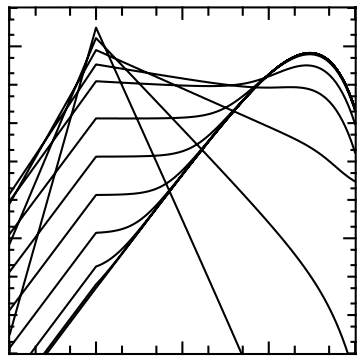

Fig. 12.7 Spectral distributions of $x^3(1-\varpi)$ times the ϖ-transform of $u(x)$ for several values of $y = (4kT/mc^2)\varpi/(1-\varpi)$.

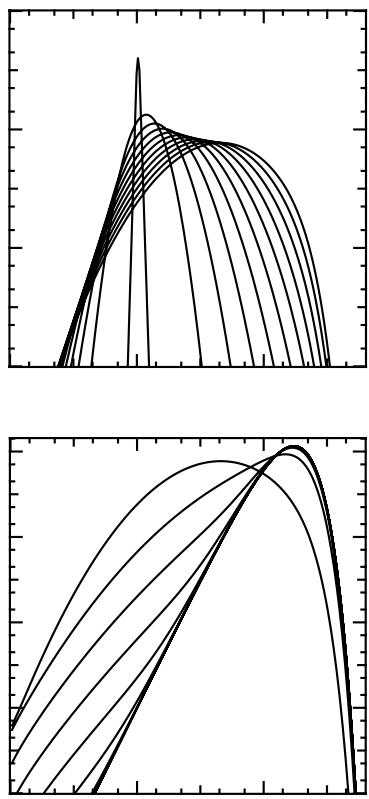

Fig. 12.8 Time-dependent spectra $x^3 n(x,t)$ vs x for Comptonization of radiation with $x_0 = 10^{-2}$. Time is expressed as values of $y = (4kT/mc^2)N_e\sigma_T ct$ ranging: (a) from 0 to 4 and (b) from 4 to 40.

$x_0 \ll x \ll 4$ at intermediate values of y, which is seen in $x^3\tilde{u}$, is not evident in the actual time-dependent spectrum. Instead the initial sharp peak at x_0 is just broadened and shifted upward in frequency with increasing t, and when the peak reaches $x \approx 1$, the further evolution consists of sharpening of the peak and depletion of the low-frequency tail, until the Wien distribution is approached.

Inverse Compton reflection is another interesting application of these same ideas. (See Lightman and Rybicki (1980), and also Rybicki and Lightman (1979), Section 7.5.) The problem to be worked out is to find the spectrum of initially low-frequency radiation that is diffusely reflected by a hot cloud, for which Compton scattering is the only process that need be considered. This is the same inverse Compton process considered above, but now the number of scatterings is not an independent variable, but has a probability distribution determined by the diffuse reflection process. Although the photons that are reflected after just a single scattering are the most numerous, the number that scatter several times, or even hundreds of times, before reemerging is not negligible, and so part of the reflected spectrum does consist of those photons that have scattered a great many times.

The method that we use to analyze this problem is, as above, to itemize the reflected flux according to the number of scatterings, and to apply to those photons that have a particular number n of scatterings the spectral distribution expected from the Kompaneets equation for that n. The probability distribution p_n of n is the part of the discussion that is new, and we will describe that in somewhat more detail.

We come back to our friend, the ϖ-transform. The generating function for p_n

$$\mathcal{F} = \sum_{n=1}^{\infty} \varpi^n p_n \tag{12.84}$$

is the diffuse reflectance – reflected flux divided by the incident flux – if the scattering is not conservative, but if instead there is a single-scattering albedo ϖ. This is one of those quantities that is calculated using the classical methods of radiative transfer theory expounded by Chandrasekhar and others. If the incident intensity is isotropic in the incoming hemisphere then Chandrasekhar's result is

$$\mathcal{F} = 1 - 2\sqrt{1-\varpi} \int_0^1 H(\mu)\mu \, d\mu \tag{12.85}$$

in terms of the standard H-function. Using a very precise subroutine to generate a table of the H-function for a few small values of ϖ allows the values of p_n to be found by estimating the numerical derivatives of $\mathcal{F}$ at $\varpi = 0$; in fact p_n is the nth derivative at $\varpi = 0$, divided by $n!$. Owing to cancellation, this method is good only for $n < 5$ or so. The values for larger n can be estimated by replacing $H(\mu)$

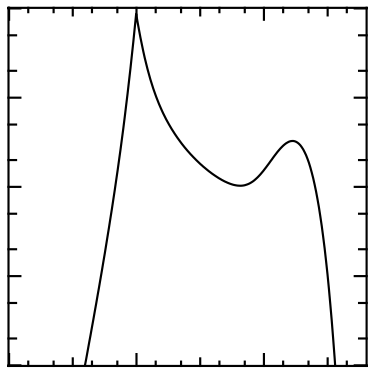

Fig. 12.9 Spectral distribution for inverse Compton reflection. Ordinate: spectral energy density $x^3 n_x$. Abscissa: $h\nu/kT$. For this case $kT = 5.11$ keV.

in (12.85) by the function for $\varpi = 1$, for which the integral has the exact value $2/\sqrt{3}$, then using the binomial theorem to expand $\sqrt{1-\varpi}$ in powers of ϖ. This gives this result for $n \gg 1$:

$$p_n \sim \frac{2}{\sqrt{3\pi}\, n^{3/2}}. \tag{12.86}$$

This has the interesting implication that something like 1% of the photons will have been scattered 10^4 or more times! The details of the numerical differentiation and of the asymptotic law can be checked using a very simple Monte Carlo code. An example of the final result is the spectrum in Figure 12.9, which is, as before, for an initial frequency $x_0 = 10^{-2}$, and here kT has the value $10^{-2} mc^2 = 5.11$ keV. In this spectrum there is a hint of a power law around $x = 10^{-1}$, and a pronounced bump at $x = 3$, the Wien peak. In this problem $4kT/mc^2$ is 0.04, so for photons to be boosted from $x_0 = 10^{-2}$ to $x = 4$ takes $\ln(400)/0.04 \approx 150$ scatterings, and 10.6% of the photons scatter at least that many times, thus populating the Wien peak.

12.4 Radiating shock waves

One of the most important situations in which the radiative energy flux works with the gas dynamics equation to produce a complex structure is in radiative shock waves. These are shocks in which the material is heated sufficiently for the radiative flux to be comparable to the flux of kinetic energy on the upwind side of the front. The classic discussion of radiating shock waves is in Zel'dovich and

Raizer (1967), Section VII.14–18; this is repeated and extended very clearly in Mihalas and Mihalas (1984), Section 104.

We have to keep in mind the dimensionless number that gives the relative importance of radiation and energy transport by mass motion. It is the Boltzmann number, or actually its reciprocal:

$$\mathrm{Bo}^{-1} = \frac{\sigma T^4}{\rho C_v T V}. \tag{12.87}$$

For the shock problem the denominator is the kinetic energy flux $(1/2)\rho_0 v_0^3$ and the temperature is estimated for scaling purposes as $(3/16)v_0^2/\mathcal{R}$, the strong shock limit for $\gamma = 5/3$. So the typical inverse Boltzmann number for a shock is $\mathrm{Bo}^{-1} = 0.0025\sigma v_0^5/\rho\mathcal{R}^4$.

Just to illustrate the numbers we quote the inverse Boltzmann number for a $100\,\mathrm{km\,s^{-1}}$ shock in gas with a preshock density of $10^{-9}\,\mathrm{g\,cm^{-3}}$; it is about 6000. Under these circumstances the influence of radiation on the shock structure is profound.

The diagnostic diagram that aids understanding the influence of radiation on the shock is the mechanical flux vs temperature diagram. This is constructed from the steady conservation laws (2.91), (2.92), and (2.96) in which viscosity is discarded but heat conduction is replaced by a more general radiation flux:

$$\rho v = C_1, \tag{12.88}$$

$$\rho v^2 + p = C_2, \tag{12.89}$$

$$\rho v e + \frac{1}{2}\rho v^3 + pv + F = C_5. \tag{12.90}$$

We divide the second equation by the first to get

$$\frac{p}{\rho} = v\left(\frac{C_2}{C_1} - v\right) = \mathcal{R}T. \tag{12.91}$$

In the third equation we assume the ideal gamma-law relation $e = (3/2)p/\rho$, so pressure and density can be eliminated to express the flux in terms of v:

$$v\left(\frac{5}{2}\frac{C_2}{C_1} - 2v\right) = \frac{C_5 - F}{C_1}. \tag{12.92}$$

Far upstream from the shock F may have an asymptotic value F_∞. The value of C_2/C_1 is v_*, the stagnation velocity. The value of C_5 is F_∞ plus an amount that is close to $v_0^2/2 \approx C_2^2/2C_1^2$ for a large Mach number. The diagnostic diagram is the plot of the left-hand side of (12.92) vs the left-hand side of (12.91).

Figure 12.10(a) illustrates the diagnostic diagram in the absence of radiation. The initial upstream state is point A at zero temperature – negligible compared

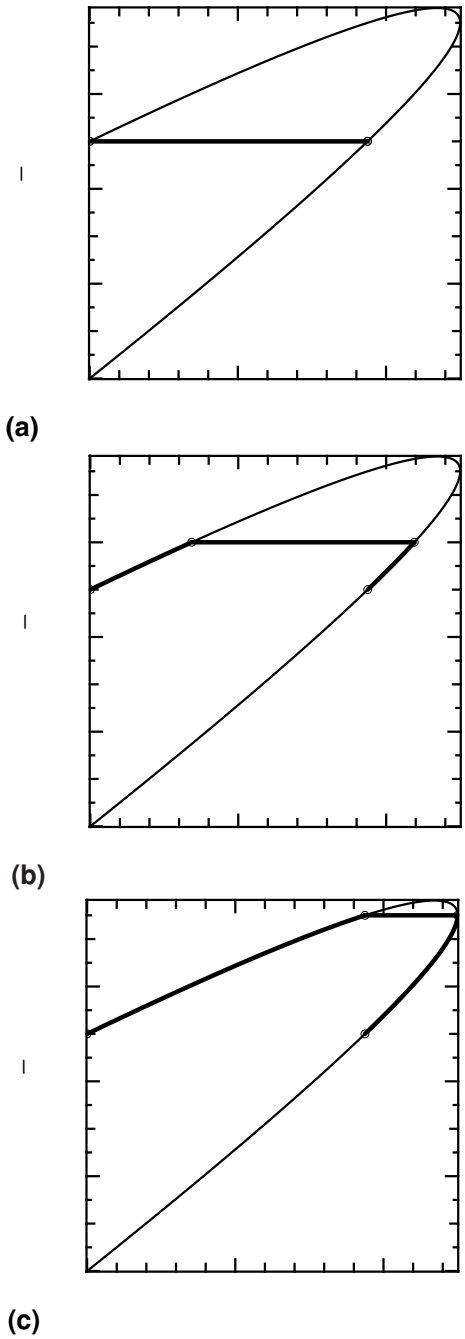

Fig. 12.10 (a) Flux vs T within a nonradiating shock. Bold lines are traversed; (b) similar for a subcritical radiating shock; (c) similar for a supercritical shock.

to the stagnation temperature $v_*^2/\mathcal{R}$ for high Mach number – and at a flux value corresponding to $(1/2)\rho v_*^3$. Across the shock there is no jump in flux, since that is one of the Rankine–Hugoniot conditions, and point B, even with point A but on the subsonic branch, represents the downstream state. The postshock temperature is 3/16 in units of the stagnation temperature.

Figure 12.10(b) illustrates the case in which there is a moderate amount of radiation present. Both the upstream and downstream regions are optically thick to the radiation that is produced within the shock, and therefore by moving far enough from the shock in each direction we can reach points A and B where the flux is negligible. These points define the values of the constants C_1 and C_2, and it is at point A where the temperature is very small in comparison with the stagnation temperature. The points A and B therefore obey the Rankine–Hugoniot conditions. But consider now what happens as we approach the shock through the preshock region. As the radiative flux from the shock becomes noticeable, representing a flux from downstream toward upstream and therefore negative the way we have defined it, the value of $C_5 - F$ becomes larger than it was, and therefore the point representing the conditions in the diagnostic diagram moves upward and to the right along the supersonic branch. For this shock the actual gas-dynamic discontinuity occurs at the point C. The jump across the discontinuity must again be horizontal in the diagram, because the radiative flux is actually continuous. This assumes we look at the flux "in the small", i.e., on a scale smaller than the radiation mean free path, and therefore since the intensity has no discontinuity neither does the flux. Thus the radiating shock structure is a shock-within-a-shock. The remote upstream and downstream conditions obey one set of Rankine–Hugoniot relations, and the observer at a great distance thinks these are "the" pre- and post-shock conditions. But within the shock, when we look closely, there is the gas-dynamic shock with another set of Rankine–Hugoniot relations. In the flow downstream from the inner shock the hot material produces emission, i.e., $dF/dx > 0$, which means that F goes up (toward zero) and therefore the point on the diagnostic diagram goes down and to the left, on the subsonic branch this time. When the material stops emitting, and the flux is restored to zero, we again arrive at point B, the eventual downstream state. We see that the amount of flux absorbed within the upstream part of the flow just equals the flux emitted within the downstream region.

Figure 12.10(c) illustrates what is called a supercritical shock, in which the amount of radiation is considerably more than in the previous case. This actually produces the situation in which the postshock temperature at the inner shock is driven up to almost exactly the maximum possible value, 1/4 of the stagnation temperature. Point C cannot rise any higher than that on the supersonic branch, since there would be nowhere for point D to go. What this does to the shock structure

we will see shortly. In the postshock cooling region the temperature recovers to point B as before. Now you will notice that point C is at exactly the same temperature as point B. This is remarkable. The precursor heating due to the radiation produced within the cooling zone raises the preshock temperature up to *just what the downstream temperature would have been without radiation*. The actual postshock temperature is made hotter than this, and only after the postshock cooling has occurred does the downstream material return to this temperature. If any attempt is made to get more radiation than this out of the shock by turning up various parameters or whatever, there is no further change in these temperatures. All that happens is that the shock adjusts the structure of the precursor region and the cooling region so that the right amounts of energy are produced and absorbed to give these temperatures.

This radiating shock structure can be analyzed in a rough way that necessarily ignores the important nonlinearities but catches the main qualitative features. The idea is to observe that the supersonic and subsonic branches of the diagnostic curve are both vaguely linear with a positive slope. In fact the slopes, $-dF/d(p/\rho\mathcal{R})$, are equal to C_1C_v and C_1C_p in the supersonic and subsonic limits, respectively, where C_v is the specific heat at constant volume and C_p is the specific heat at constant pressure. So let us forget about the nonlinearity and use a linear formula connecting F and T, but perhaps with different slopes if we like. We do also need to put in the offset: the (radiative) flux goes to zero at $T = 0$ in the supersonic branch, but it goes to zero at point B in the subsonic branch, where $T = T_0$ is large. We will use the value $aT_0^4 = E_0$ below. What we actually want is a linear relation between the flux and the equilibrium energy density, aT^4. We express that slope as

$$\frac{daT^4}{dF} = 4aT^3\frac{dT}{dF} = -\frac{4aT^3}{C_1C} = -\frac{16\sigma T^4}{cC_1CT}. \tag{12.93}$$

We adopt the Eddington approximation (*not* thermal diffusion) for which

$$F = -\frac{c}{3\kappa_R\rho}\frac{dE}{dx}, \tag{12.94}$$

so the coefficient of the relation between aT^4 and $(1/\kappa_R\rho)dE/dx$ is $16\sigma T^4/3C_1CT$. Apart from the factor 16/3 this is the inverse of the Boltzmann number. As mentioned above, the specific heat C is smaller in the supersonic region than it is in the subsonic region by a factor $\gamma = 5/3$; we will not worry about this minor inaccuracy since the nonlinearity of the relation between aT^4 and T is

much more serious. Finally we adopt these linear relations between aT^4 and F:

$$aT^4 = \begin{cases} \dfrac{\mathrm{Bo}^{-1}}{\kappa_R \rho}\dfrac{dE}{dx} & \text{upstream} \\ E_0 + \dfrac{\mathrm{Bo}^{-1}}{\kappa_R \rho}\dfrac{dE}{dx} & \text{downstream} \end{cases} . \tag{12.95}$$

The next step is to solve the Eddington approximation equation of transfer given that aT^4 is obtained from these linear relations. Keeping to the spirit of this crude model we will not be concerned with the variation of the absorptivity with location within the shock – a large effect in reality – and thus make all the coefficients spatially constant. The Eddington equation for E is then

$$\frac{d^2E}{dx^2} = \begin{cases} 3(\kappa_R\rho)^2\left(E - \dfrac{\mathrm{Bo}^{-1}}{\kappa_R\rho}\dfrac{dE}{dx}\right) & \text{upstream} \\ 3(\kappa_R\rho)^2\left(E - E_0 - \dfrac{\mathrm{Bo}^{-1}}{\kappa_R\rho}\dfrac{dE}{dx}\right) & \text{downstream} \end{cases} . \tag{12.96}$$

The homogeneous equation has exponential solutions $E \sim \exp(px)$, and the roots for p are found to be

$$\frac{p}{\kappa_R\rho} = -\frac{3}{2\mathrm{Bo}} \pm \left[3 + \left(\frac{3}{2\mathrm{Bo}}\right)^2\right]^{1/2} . \tag{12.97}$$

These roots tell an interesting story. The positive one has to be used upstream and the negative one downstream. When the Boltzmann number is large – weak radiation – the roots are the usual $\pm 1/\sqrt{3}$ and the radiation extends symmetrically one mean free path or so in each direction. But in the strong-radiation case the roots are very unequal. The positive root goes to $\mathrm{Bo}\kappa_R\rho$ while the negative one goes to $-3\kappa_R\rho/\mathrm{Bo}$. So on the upstream side the extent of the radiation is very large, of order Bo^{-1} mean free paths, but on the downstream side the radiation drops very abruptly, in Bo mean free paths. The very sharp cooling zone behind the shock means that the thermal diffusion approximation is hopeless there; it just gives the wrong answer.

We can find the correct solutions now. We put in adjustable coefficients for the exponentials, and try these solutions:

$$E = \begin{cases} E_a \exp(p_a x) & \text{upstream} \\ E_0 + E_b \exp(p_b x) & \text{downstream} \end{cases} , \tag{12.98}$$

where p_a is the positive root and p_b is the negative root. We have to find the constants E_a and E_b by matching the values of E and F at the shock. (The second

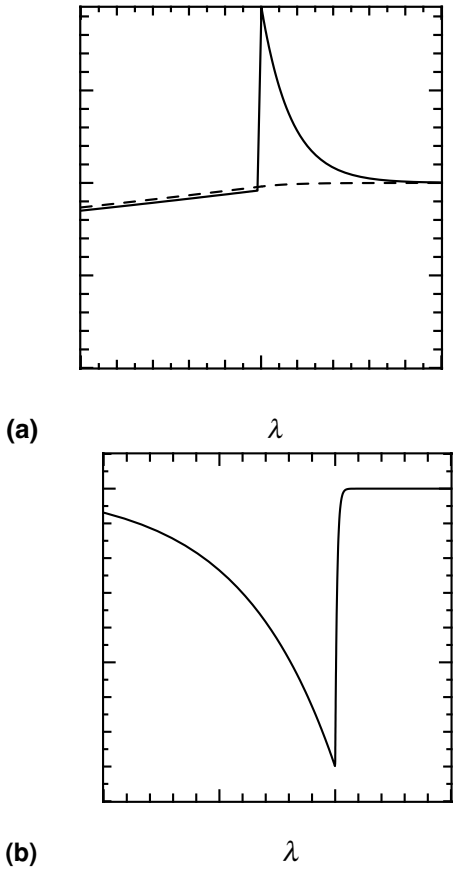

Fig. 12.11 (a) Distributions of radiation density E (dashed) and equilibrium radiation density aT^4 (solid) vs x for a shock with Bo $= 1/4$; (b) the corresponding distribution of flux.

derivative is discontinuous since aT^4 is discontinuous.) The results are

$$E_a = E_0 \frac{p_b}{p_b - p_a}, \tag{12.99}$$

$$E_b = E_0 \frac{p_a}{p_b - p_a}. \tag{12.100}$$

Since p_a is positive and p_b is negative, E_a will be positive and E_b will be negative. This means that E increases monotonically with x through the shock, so the flux is in the $-x$ direction everywhere. The flux follows from (12.94) and the distribution of aT^4 (i.e, of temperature) follows from (12.95).

A sample of what the solutions look like is shown in Figure 12.11. The runs of E and aT^4 track fairly closely with the notable exception of the temperature spike behind the shock, which, because it is quite optically thin, has almost no

influence on E. The flux profile is shown on a wider range of x to illustrate the very great extent of the precursor. On this scale the jump in flux at the shock appears discontinuous, but it is not. The length scale for F to rise from its minimum value at the front toward zero is about one tenth of a mean free path, the same as the width of the cooling region. It should be noted that this value of the inverse Boltzmann number, 4, is quite modest. With $\mathrm{Bo}^{-1} \approx 6000$ the precursor and temperature spike length scales are orders of magnitude different. Or, they would be if some neglected physical processes did not change the scale. The predicted width of the spike is comparable with the scale lengths for some of the very fastest plasma processes: electron–ion coupling, collisional ionization, and shorter than some, such as that for radiative recombination. Calculating the shock structure in detail requires the most involved kind of plasma transport modeling, and the modeling work has probably not yet been carried out with sufficient thoroughness to give a satisfactory account of some of the excellent laboratory experiments.

The final remarks about radiating shocks concerns the effect of frequency-dependent opacity, and in particular the effect of very opaque parts of the spectrum with quite transparent windows between. A model based on the Rosseland mean is not adequate to catch the main features in this case. The reason there can be a qualitative difference with and without a spectral window to the outside world is that the existence of the window makes it possible for the hot postshock material to cool down to the original temperature of the upstream gas. That is, there is an "outside world" temperature bath and the spectral window makes it possible for the postshock gas to equilibrate to it. The structure close to the shock is not modified as much, although the actual length scales represent averages over different opacities and differ from those in the gray opacity model. In the diagnostic diagram the new qualitative feature is that from point B the postshock cooling flow proceeds on down in temperature until a value near zero is reached. The final state and the starting state A are connect by the isothermal jump conditions, which conserve mass, momentum and temperature, replacing energy.

It is helpful to remember these relations for isothermal shocks:

$$\rho_0 v_0 = \rho_1 v_1, \tag{12.101}$$

$$p_0 + \rho_0 v_0^2 = p_1 + \rho_1 v_1^2, \tag{12.102}$$

$$\frac{p_0}{\rho_0} = \frac{p_1}{\rho_1} = a^2, \tag{12.103}$$

from which we see that

$$\frac{v_0}{a} = \frac{a}{v_1} = M, \tag{12.104}$$

the Mach number (relative to the isothermal sound speed), so the density ratio is

$$\frac{\rho_1}{\rho_0} = M^2. \tag{12.105}$$

The formation of isothermal shocks in the relatively dense atmospheres of pulsating stars and the difference in the way they develop with height compared with adiabatic shocks is a significant topic for pulsating star physics, which we cannot discuss here. It should be noted that not all shocks in material that has spectral windows will be isothermal. This requires that the emissivity of the hot shocked matter be sufficiently large that the length scale for the cooling is short compared with the larger problem dimensions. This is a statement about the density of the shocked material. As a shock propagates upward through a density gradient spanning orders of magnitude it may first be adiabatic because even the spectral windows are opaque enough to block the escape of radiation; then there may be an isothermal propagation phase, because the radiation escapes but the cooling length scale is still short compared with other dimensions; finally the shock is adiabatic again because the cooling processes are inefficient. These transitions in shock behavior form one of the most interesting aspects of studying pulsating stars.

12.5 Radiatively driven stellar winds

The final example to be discussed is the theory of radiatively-driven stellar winds. The astrophysical motivation is the existence in some stars, and perhaps in active galactic nuclei, molecular clouds and some circumstellar outflows, of supersonic motions that are combined with spectral line transport. The momentum deposited by the line radiation is certainly important in some of these cases. We have already studied how to approximately solve the transport equation in the Sobolev, large velocity gradient, approximation, and we found an expression for the body force on the material due to radiation pressure in spectral lines treated in this approximation.

The theory for radiatively-driven winds presented here is the CAK theory, from Castor *et al.* (1975). There has been considerable elaboration of the theory since 1975, and the current state can be found in the articles presented in Howarth (1998). A particularly rich vein has been the study of the instability of radiative driving. Some of the current work was reviewed at the conference in Isle-aux-Coudres, Quebec (Moffat, Owocki, Fullerton, and St. Louis, 1995) The hydrodynamics of the instabilities has been studied with increasing precision, and now the association between radiation-driven instabilities and the x-ray emission from the winds is secure (Feldmeier *et al.*, 1997).

The application of the Sobolev line force result (6.117) to stellar winds is made much easier than it would otherwise be by a remarkable empirical fact about large

databases of line opacity data: *line opacities are distributed approximately as a power law.* The values of k_L that determine the Sobolev optical depth have been found to follow this law for the number of lines stronger than a given value of k_L:

$$N(k_L) = N_0 k_L^{\alpha-1}. \tag{12.106}$$

The constant α in the exponent ranges between 0.5 and 0.7 depending on the database. When the lines are all added up it is found that the total body force, or radiative acceleration, varies in this way in the radial beaming approximation:

$$g_R = \frac{\kappa_T F}{c} k \left(\frac{1}{v_{\rm th} \kappa_T \rho} \frac{du}{dr} \right)^{\alpha}. \tag{12.107}$$

The proportionality factor k is related to the normalizing constant N_0 in the line distribution. The other factors is this formula have been introduced to make certain of the variables dimensionless. Among these, κ_T is the Thomson opacity $N_e \sigma_T / \rho$ and $v_{\rm th}$ is a representative value of the rms velocity of the absorbing ions. F is the total flux. This α-power law is a result of blending optically thin lines for which the force is proportional to F with thick lines for which it is proportional to $(F/\rho) du/dr$.

The stellar wind equations including the radiative driving force are variations of (12.16) and (12.17) in which the temperature gradient term in the latter is omitted (the thermal pressure turns out to be a relatively small effect in setting the structure of the wind), and the radiative acceleration is included instead. When the density is eliminated this equation is found for the flow speed:

$$\left(u - \frac{a^2}{u} \right) \frac{du}{dr} - \frac{2a^2}{r} + \frac{G\mathcal{M}}{r^2} - \frac{C}{r^2} \left(r^2 u \frac{du}{dr} \right)^{\alpha} = 0. \tag{12.108}$$

The factor C is a collection of constants,

$$C = \frac{\kappa_T L k}{4\pi c} \left(\frac{4\pi}{\kappa_T v_{\rm th} \dot{\mathcal{M}}} \right)^{\alpha}; \tag{12.109}$$

it is the eigenvalue that is related to the mass-loss rate. The isothermal sound speed is treated as a constant since the flow is expected to be nearly isothermal for the same reasons discussed in the previous section. The boundary conditions are that the velocity should be sonic – small in comparison with the final velocity – somewhere near the stellar photosphere, and the flow should keep going beyond the Parker radius $r = G\mathcal{M}/2a^2$. The analysis is somewhat tricky, and has become generally accepted only after being corroborated by much more elaborate calculations.

The analysis in question examines the locus of points in the r–u plane where this nonlinear differential equation is singular. If the equation is written in this

form, in which du/dr is denoted by u',

$$F(r, u, u') = 0, \tag{12.110}$$

then a singular point is a point (r, u), where this algebraic equation is not solvable for u'. The condition for solvability is a nonvanishing partial derivative with respect to the variable to be solved for, so singular points are those points that obey

$$\frac{\partial F}{\partial u'} = 0. \tag{12.111}$$

When u' is eliminated between (12.110) and (12.111) the result is a single equation that connects u and r. This defines the *singular locus* for this differential equation. This is more general than the sonic point that occurs in Parker's wind theory (Parker, 1960), for example, or in the transonic evaporation model discussed earlier. In fact, the sonic point is *not* one of the singular points since (12.110) is solvable there. The rest of the mathematical argument is based on the assertion that an acceptable solution can only begin with a small u near the photosphere and reach large radius with a large velocity if it grazes the singular locus at one point. The solutions that miss the singular locus entirely either do not exist with $u < a$ or cease to exist at $r > G\mathcal{M}/2a^2$. "Grazing" the singular locus means touching it at a point of tangency. Solution curves that meet it at a nonzero angle form a cusp at that point and stop. The condition for tangency is found by differentiating (12.110) with respect to radius and then substituting (12.111):

$$\frac{dF}{dr} = \frac{\partial F}{\partial r} + u'\frac{\partial F}{\partial u} + u''\frac{\partial F}{\partial u'} = \frac{\partial F}{\partial r} + u'\frac{\partial F}{\partial u} = 0. \tag{12.112}$$

We call this the regularity condition.

We can now pick any value for the radius of this regular critical point, *not* the sonic point, and solve the three equations (12.110), (12.111), and (12.112) for the three unknowns u, u', and C. Then numerical integrations beginning from this point give the complete solution, including the run of density since C fixes the mass-loss rate. If the photospheric radius computed using this flow model is not the desired one, the hypothesized critical point radius can be adjusted until it is.

We will give the simplest version of these steps, as in Castor *et al.* (1975). The equation for $F = 0$ is

$$\left(u - \frac{a^2}{u}\right) r^2 \frac{du}{dr} - 2a^2 r + G\mathcal{M} - C\left(r^2 u \frac{du}{dr}\right)^{\alpha} = 0. \tag{12.113}$$

The derivative with respect to du/dr is

$$\left(u - \frac{a^2}{u}\right) r^2 - \frac{\alpha}{du/dr} C\left(r^2 u \frac{du}{dr}\right)^{\alpha} = 0, \tag{12.114}$$

and the regularity equation is

$$\left(u-\frac{a^2}{u}\right)2r\frac{du}{dr}-2a^2-\frac{2\alpha}{r}C\left(r^2u\frac{du}{dr}\right)^{\alpha}$$
$$+\left(1+\frac{a^2}{u^2}\right)r^2\left(\frac{du}{dr}\right)^2-\frac{\alpha(du/dr)}{u}C\left(r^2u\frac{du}{dr}\right)^{\alpha}=0. \quad (12.115)$$

We consider these equations first in the hypersonic $a=0$ limit. The first two equations become

$$r^2u\frac{du}{dr}+G\mathcal{M}-C\left(r^2u\frac{du}{dr}\right)^{\alpha}=0, \quad (12.116)$$
$$r^2u\frac{du}{dr}-\alpha C\left(r^2u\frac{du}{dr}\right)^{\alpha}=0, \quad (12.117)$$

which have the solution

$$r^2u\frac{du}{dr}=\frac{\alpha}{1-\alpha}G\mathcal{M}, \quad (12.118)$$
$$C\left(r^2u\frac{du}{dr}\right)^{\alpha}=\frac{1}{1-\alpha}G\mathcal{M}. \quad (12.119)$$

To locate the actual singular point we need to consider the small quantities proportional to a^2. We first express the second of the three original equations as

$$r^2u\frac{du}{dr}-\alpha C\left(r^2u\frac{du}{dr}\right)^{\alpha}=a^2r\frac{r}{u}\frac{du}{dr}. \quad (12.120)$$

The regularity equation is written as

$$\left[r^2u\frac{du}{dr}-\alpha C\left(r^2u\frac{du}{dr}\right)^{\alpha}\right]\left[\frac{2}{r}+\frac{1}{u}\frac{du}{dr}\right]=2a^2\left(\frac{r}{u}\frac{du}{dr}+1\right)-a^2\left(\frac{r}{u}\frac{du}{dr}\right)^2. \quad (12.121)$$

Combining the last two equations leads to

$$r\frac{r}{u}\frac{du}{dr}\left[\frac{2}{r}+\frac{1}{u}\frac{du}{dr}\right]=2\left(\frac{r}{u}\frac{du}{dr}+1\right)-\left(\frac{r}{u}\frac{du}{dr}\right)^2, \quad (12.122)$$

or

$$\left(\frac{r}{u}\frac{du}{dr}\right)^2=1. \quad (12.123)$$

We take the positive root,

$$\frac{r}{u}\frac{du}{dr} = 1. \tag{12.124}$$

All the critical point data are now determined, given a choice of the critical point radius. It remains to relate this to the photospheric radius. We consider again the $a = 0$ limit. The differential equation (12.116) in that limit *has only a single root for* $r^2 u du/dr$ that is independent of what r and u may be. In other words, the entire solution for $u \gg a$ is described by

$$u = \left[\frac{2\alpha G\mathcal{M}}{(1-\alpha)R_*}\left(1 - \frac{R_*}{r}\right)\right]^{1/2}. \tag{12.125}$$

With this solution the critical point, which is where the slope obeys (12.123), is at

$$\frac{r_c}{R_*} = \frac{3}{2}. \tag{12.126}$$

It has been discovered that mild changes in the way the temperature is distributed with height have hardly any effect on the velocity law (12.125) but change the location of the critical point.

Equation (12.125) provides the scaling law for the terminal velocity of the wind: it is proportional to the star's escape velocity. The formula for C (derived from (12.118) and (12.119))

$$C = \alpha^{-\alpha}(1-\alpha)^{-(1-\alpha)}(G\mathcal{M})^{1-\alpha} \tag{12.127}$$

gives the mass-loss rate

$$\dot{\mathcal{M}} = \left(\frac{4\pi G\mathcal{M}}{\kappa_T v_{\rm th}}\right)\alpha(1-\alpha)^{(1-\alpha)/\alpha}\left(\frac{k\kappa_T L}{4\pi G\mathcal{M}c}\right)^{1/\alpha}, \tag{12.128}$$

in which L is the stellar luminosity.

The predictions of this theory are found to be in fair quantitative agreement with the winds of hot stars. Two notable features are the scaling of u_∞ with escape velocity and the dependence of the mass-loss rate on a power somewhat larger than unity of the stellar luminosity. The agreement is improved if the radial-beaming approximation for g_R is replaced with a proper integration over the cone of photospheric radiation. (See Friend and Castor (1983), Pauldrach, Puls, and Kudritzki (1986), Friend and Abbott (1986) and Kudritzki, Pauldrach, Puls, and Abbott (1989).) This increases the terminal velocity and softens the steepness of the velocity law at $r \gtrapprox R_*$, both of which improve the agreement with observations. The more recent detailed calculations of excitation and ionization balance in the stellar wind models have made the calculations of g_R more reliable without

changing the basic results much. The most recent work in stellar wind theory concerns the instability of radiative driving and the large-scale high velocity shocks that are produced as a result. Unfortunately space does not allow a discussion of that work here, but see the IAU Colloquium volume *Variable and Non-spherical Stellar Winds in Luminous Hot Stars* (Wolf, Stahl, and Fullerton, 1998) for reports of the status in 1998.